ACS APPLIED MATERIALS & INTERFACES

www.acsami.org

Research Article

Temperature and Thickness Dependence of the Thermal Conductivity in 2D Ferromagnet Fe_3GeTe_2

Marcel S. Claro,* Javier Corral-Sertal, Adolfo Otero Fumega, Santiago Blanco-Canosa, Manuel Suárez-Rodríguez, Luis E. Hueso, Victor Pardo,* and Francisco Rivadulla

Cite This: *ACS Appl. Mater. Interfaces* 2023, 15, 49538−49544

Read Online

ACCESS | Metrics & More | Article Recommendations | Supporting Information

ABSTRACT: The emergence of symmetry-breaking orders such as ferromagnetism and the weak interlayer bonding in van der Waals materials offers a unique platform to engineer novel heterostructures and tune transport properties like thermal conductivity. Here, we report the experimental and theoretical study of the cross-plane thermal conductivity, $\kappa_\perp$, of the van der Waals two-dimensional (2D) ferromagnet Fe_3GeTe_2. We observe an increase in $\kappa_\perp$ with thickness, indicating a diffusive transport regime with ballistic contributions. These results are supported by the theoretical analyses of the accumulated thermal conductivity, which show an important contribution of phonons with mean free paths between 10 and 200 nm. Moreover, our experiments show a reduction of $\kappa_\perp$ in the low-temperature ferromagnetic phase occurring at the magnetic transition. The calculations show that this reduction in $\kappa_\perp$ is associated with a decrease in the group velocities of the acoustic phonons and an increase in the phonon−phonon scattering of the Raman modes that couple to the magnetic phase. These results demonstrate the potential of van der Waals ferromagnets for thermal transport engineering.

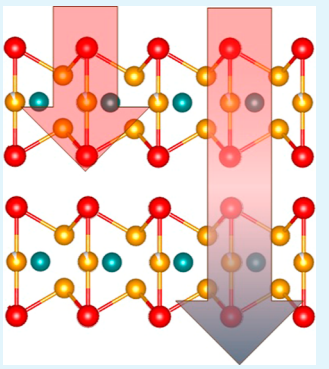

KEYWORDS: *thermal conductivity, van der Waals, 2D materials, ferromagnetism, thermoreflectance*

INTRODUCTION

The electric-field control of the conductivity of atomic-thick graphene,[1,2] shortly afterward extended to $NbSe_2$ and MoS_2,[3] opened up new possibilities for material properties manipulation in the novel world of two-dimensional (2D) van der Waals (vdW) materials and heterostructures.[4] Particularly, on vdW materials, the extreme bonding anisotropy is translated into a giant anisotropy also in the thermal transport, where the in-plane thermal conductivity $\kappa_\parallel$ is much larger than the cross-plane one $\kappa_\perp$,[5] despite the prediction of phonon mean-free paths (mfp) of the order of several tens of nanometers across the weakly bonded planes.[6,7] Defects and imperfect layer stacking result in a mixed contribution of ballistic transport (large mfp, coherent phonons) and diffusive transport (small mfp), which reduces very much the thermal conductivity across the 2D planes.[6,8]

Thermal transport is a crucial aspect for developing functional devices, which rely on an efficient heat dissipation to the base substrate, in a process determined by the thermal conductivity of the material itself and the thermal boundary conductance (TBC) of the interface with the substrate.[9,10]

A particularly interesting 2D material regarding heat dissipation is the itinerant ferromagnet Fe_3GeTe_2 (FGT): charge doping through Li^+-intercalation modulates its magnetic anisotropy and increases T_C up to room temperature,[11] while a strong spin-phonon coupling[12] produces a significant effect of magnetic ordering on the thermal conductivity, opening the door to gate-tunable 2D thermal devices. First-principles calculations in other 2D magnetic materials, like 2H−VSe_2, CrI_3, FeX_3, and RuX_3 (X = Cl, Br, and I),[13−16] have predicted a large change of the thermal conductivity in their magnetically ordered phase as well, although an experimental confirmation of such a large switching of the thermal conductivity associated with magnetic ordering in 2D materials is lacking.

In this work, we report experimental measurements combined with a theoretical analysis of the thickness and temperature dependence of the thermal conductivity in FGT. We have observed an increase in the cross-plane thermal conductivity with thickness, characteristic of a mixed ballistic propagation of long mfp phonons with diffusive transport, as well as a large drop in the thermal conductivity in the magnetically ordered phase. Both effects can be understood by our ab initio analysis of the thermal conductivity based on density functional theory (DFT) calculations.

RESULTS AND DISCUSSION

FGT is a 2D itinerant ferromagnet with $T_C \approx 200$ K, which decreases with the number of layers but retains the magnetic

Received: August 5, 2023
Accepted: October 2, 2023
Published: October 17, 2023

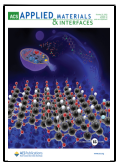

order down to the single-layer limit.[17] Neutron diffraction data support a ferromagnetic (FM) order also along the *c*-axis,[18] although theoretical calculations and analysis of experimental magnetic susceptibility suggested an antiferromagnetic (AF) stacking below $T_C \approx 152$ K.[19] From the structural point of view, the material is weakly bonded off the plane via van der Waals interactions, which facilitates its mechanical exfoliation and transfer of few layer thick flakes to a substrate. The unit cell consists of two vdW planes with hexagonal symmetry, each formed by 3 Fe atomic planes (see Figure 1).

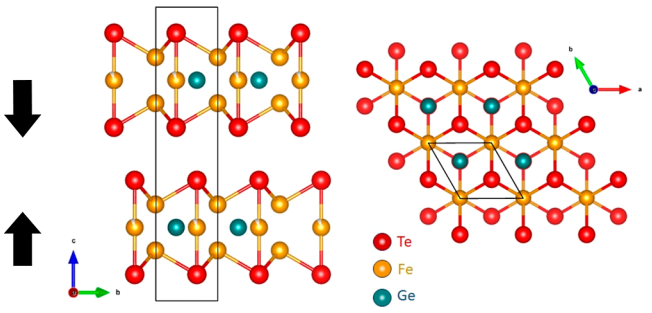

Figure 1. Crystal structure of Fe_3GeTe_2: left: lateral view of the structure. The cell is formed by two layers shifted with respect to each other. In the low-temperature magnetic phase, the layers become ferromagnetic (FM) with an antiferromagnetic interlayer coupling (as schematically shown by the arrows depicted). Right: top view of the structure showing the hexagonal symmetry of the *ab* plane. Fe, Ge, and Te atoms are shown in gold, purple, and green, respectively.

The crystals for this study were exfoliated from larger pieces obtained from HQ graphene (see Supporting Information for further details of the structural and chemical characterization of the samples). DC magnetization data of bulk crystals show that $T_C \approx 200$ K, as expected for fully stoichiometric crystals (Figure 2a shows how the zero-field-cooled and field-cooled magnetization curves separate from each other at the transition temperature). Temperature-dependent X-ray analysis shows a change in the slope of the *c*-axis parameter at T_C (Figure 2b), but no change in the space group of the crystal accompanies the transition.

Few layer thick flakes of FGT were prepared by mechanical exfoliation and transferred to (0001) sapphire substrates using PDMS stamping.[20] Transferred FGT flakes have tens of microns in lateral dimensions and thicknesses ranging from 15 to 250 nm (Figure 2c,d; see also Supporting Information). The flakes are always thicker than 5 layers, considered to be the border between 2D and 3D magnetism,[21] so that the comparison with the bulk calculations is justified.

Thermal conductivity was measured by Frequency Domain Thermoreflectance (FDTR), using a ≈60 nm thick layer of Au as a transducer[22] (see Figure S4 in the Supporting Information). To extract κ and the TBC from the FDTR phase-shift curves, we fitted the most common model wherein total energy conservation and energy transfer between layers are imposed by a transfer matrix, as explained elsewhere[23] and in the Supporting Information. The multiparameter fitting can lead to unrealistic results if several parameters are kept free and the initial guess is distant from the global minimum. To reduce the number of fitting parameters, the thickness of the Au layer was measured by X-ray reflectivity, and its thermal conductivity was estimated from the sheet electrical resistance measured by the van der Pauw method and the Wiedemann−Franz law. The thickness of the FGT flakes was measured by atomic force

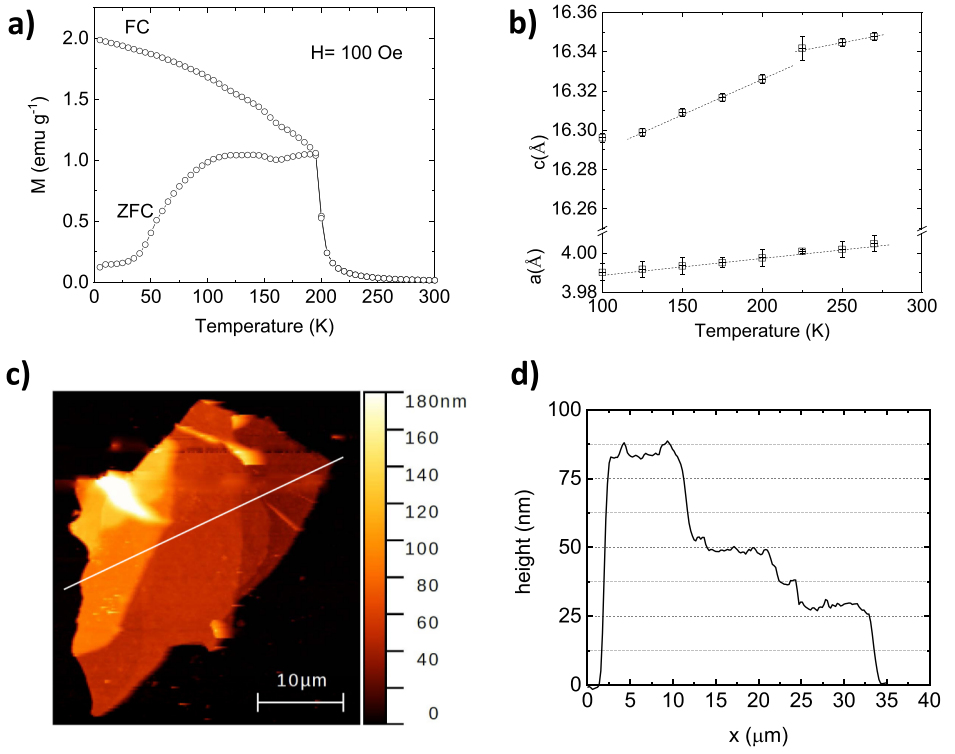

Figure 2. (a) Temperature dependence of the magnetization zero-field (ZFC) and field cooling (FC) curves measured at H = 100 Oe, and (b) lattice parameters measured for a bulk crystal of FGT. (c) Atomic force microscopy (AFM) image of one flake transferred to the surface of a (0001) sapphire substrate. The corresponding height profile along the line in panel c is shown in panel (d).

https://doi.org/10.1021/acsami.3c11578
ACS Appl. Mater. Interfaces 2023, 15, 49538−49544

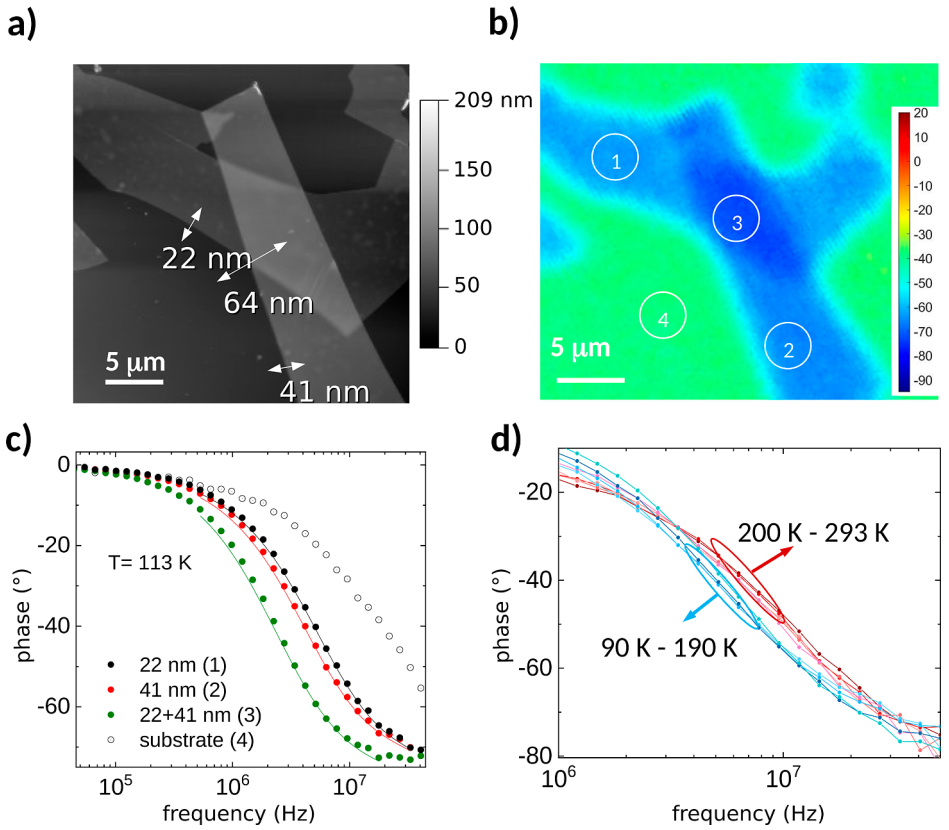

Figure 3. (a) 30 × 30 μm AFM topography of two partially overlapping flakes. (b) Phase-shift map at 20 MHz of the same region (enclosed within the square) observed in (a), with the corresponding points marked. In this image, the flakes are already covered with 60 nm of Au for the FDTR measurements. (c) Phase-shift vs frequency curves for the three points marked in (a,b), along with the fitting to the thermal model. The curve of the substrate, as a reference, is also shown. (d) Phase-shift vs frequency curves of point 2 at different temperatures. There is a large change around 200 K associated with the magnetic ordering temperature (see text).

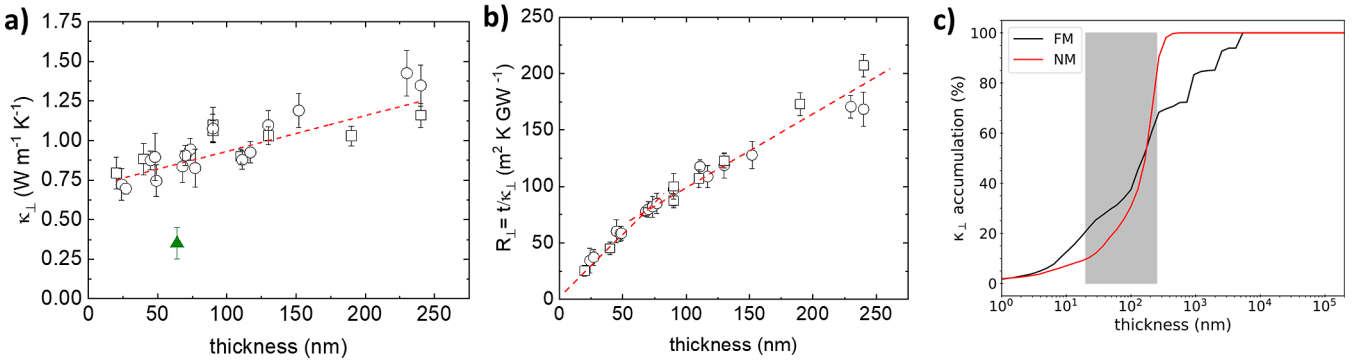

Figure 4. Measured thermal conductivity (a), and thermal resistance $R_\perp = t/\kappa_\perp$, (b) at room temperature for different flakes with varying thicknesses. Circles and squares correspond to different sets of crystals transferred to different substrates. The green solid triangle in (a) corresponds to $\kappa_\perp$ at point 3 in Figure 3a, the region of superposition of the two flakes. The dotted lines are linear fittings. (c) Accumulated $\kappa_\perp$ as a function of the phonon mean free path at 300 K. The shaded area shows the thickness range of the flakes studied by FDTR in this work.

microscopy (AFM). Heat capacities were taken from the literature, confirmed by differential scanning calorimetry (DSC), and kept fixed for each temperature in all fittings.[24] The thermal conductivity of the substrate was measured and confirmed with the values from the literature.[25] Since vdW materials present high anisotropy between the conductivity in-plane $\kappa_\parallel$ (κ_{xx}, κ_{yy}) and cross-plane $\kappa_\perp$ (κ_{zz}), their values could be considered separately in the model. However, the sensitivity to $\kappa_\parallel$ is very low, and it has a negligible influence in the $\kappa_\perp$ value (see Supporting Information Figure S4 for the sensitivity analysis). Thus, $\kappa_\parallel = \kappa_\perp$ was assumed. In this way, the free parameters in the fittings are reduced to $\kappa_\perp$ of FGT and the TBC between Au/FGT, G1, and between FGT/Al_2O_3, G2. We considered the initial values for G1 ≈ 30−40 MW m^{-2} K^{-1}, similar to Au/MoS_2,[6] and G2 ≈ 25 MW m^{-2} K^{-1}, as reported for MoS_2/Al_2O_3,[26] and MoS_2/SiO_2[6] interfaces.

On the other hand, the variability of G2 between mechanically transferred flakes may be an important source of error. For that reason, multilayer flakes like those shown in Figure 2c are important to reduce problems associated with the variability of G2, as they allow the measurement of $\kappa_\perp$ for

https://doi.org/10.1021/acsami.3c11578
ACS Appl. Mater. Interfaces 2023, 15, 49538−49544

different thicknesses with the same FGT/sapphire interface (see also Figure S3 in the Supporting Information).

Initial values of $\kappa_\perp$ of 1 Wm^{-1} K^{-1}, typical for other 2D materials, were used for an estimation of the sensitivity to different parameters in different frequency ranges. The spot size was varied between a $1/e^2$ diameter ≈ 4 and 11 μm for achieving better sensitivity to TBC and $\kappa_\perp$. The fittings shown in Figure 3c to obtain the $\kappa_\perp$ and TBCs reported in this work were performed from 1 to 50 MHz, where the sensitivity for these parameters is maximum (see Figure S4 in the Supporting Information).

Figure 3a shows the AFM topography of two partially overlapping flakes of thicknesses 22 and 41 nm, respectively. The 30 × 30 μm phase shift map at 20 MHz shows the variations in the contrast due to the differences in $\kappa_\perp$ and TBC. The whole frequency phase-shift spectra for each point marked in (a,b) are presented in Figure 3c,d at different temperatures, demonstrating good sensitivity to thickness and temperature.

The thickness dependence of $\kappa_\perp$ at room temperature is shown in Figure 4a. To reduce errors from sample preparation and defects, several flakes were measured, and each flake was measured several times. Thus, the error bars represented in the figure are obtained from the statistical variance. In this figure is observed an increase of $\kappa_\perp$ with the thickness of the sample, of the order of ≈0.5 W/m K in a range of ≈200 nm. Although small, this is of the same order of magnitude as that reported for other van der Waals materials, like MoS_2[6] or $SnSe_2$,[27] and it is consistent with our DFT calculations for FM and nonmagnetic (NM) phases (Figure S11 of Supporting Information). The calculated accumulated $\kappa_\perp$; Figure 4c) shows that more than 50% of the heat at 300 K is carried by phonons with a mean-free path larger than ≈200 nm, suggesting an important contribution from ballistic phonons along the *c*-axis, as in other vdW structures.[6,28]

In the case of pure ballistic transport, phonons can propagate without thermal resistance inside the material so that $R_\perp = R_{int} + t/\kappa_\perp$ should be a constant, independent of thickness. However, the measured experimental cross-plane thermal resistance, $R_\perp$, also increases with the thickness (Figure 4b). On the other hand, in a purely diffusive regime, $R_\perp(t)$ is linear with a constant slope = $1/\kappa_\perp$.[8] For FGT, $R_\perp$ increases linearly with thickness above ≈60 nm, giving $\kappa_\perp \approx$ 1.9(1) Wm^{-1} K and $R_{int} \approx 46$ m^2 K/GW, but it deviates from this behavior for thinner samples, with a vanishing resistance as $t \to 0$. The change in slope suggests some thickness-dependent contribution, and although the data in Figure 4b seem to extrapolate to zero, the thinner samples measured in this work are $t \approx 25$ nm, so we cannot exclude a small finite value of $R_\perp$ close to the monolayer limit (note that a residual value as small as ≈10 m^2 K/GW has been reported for a few monolayers of MoS_2).[6]

We have also measured $\kappa_\perp$ in the superposition region of two crystals, point 3 in Figure 3a: $\kappa_\perp$ is substantially reduced in the overlapping region of total thickness 63 nm (green triangle in Figure 4a). Actually, the phase-shift curve of point 3 can be fitted with two layers, of 22 and 41 nm each, with their corresponding $\kappa_\perp$, and a high interlayer thermal resistance between both flakes of ≈180 m^2 K/GW (TBC ≈ 10−12 MW m^{-2} K^{-1}). The value of the TBC between the two FGT flakes is of the same order of magnitude as reported for interfaces between dissimilar 2D materials, like graphene/MoS_2 or MoS_2/WSe_2,[9] although in this case, the large interfacial resistance occurs between films of the same composition without any mass density or compositional mismatch.

Finally, the experimental temperature dependence of $\kappa_\perp$ is shown in Figure 5a for two different thicknesses (points 1 and

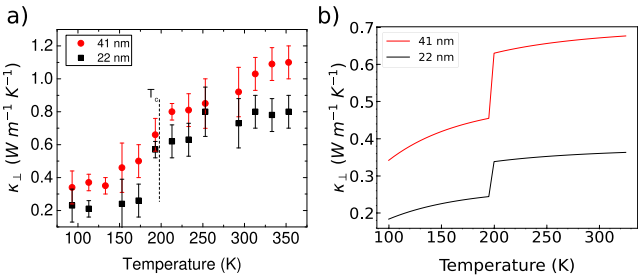

Figure 5. Experimental (a) and theoretical (b) temperature dependence of the thermal conductivity of two flakes with thicknesses 22 and 41 nm, corresponding to points 1 and 2 in Figure 3a, respectively. (b) Calculated temperature dependence of $\kappa_\perp$ for the NM and FM phase of bulk FGT, considering the NM (FM) phase above (below) the experimental value of the magnetic transition temperature.

2 in Figure 3a). A reduction of $\kappa_\perp$ between 25 and 65% occurs below T_C in the transition to the magnetic phase. Note that the jump in $\kappa_\perp$ is clearly observed in the raw phase-shift curves (Figure 3d) and, therefore, cannot be attributed to fitting artifacts.

It is common in magnetic and ferroelectric materials that the formation of domain walls causes a reduction of thermal conductivity due to phonon scattering on domain boundaries.[29,30] However, the $\kappa_\perp$ obtained is robust to external magnetic fields up to 50 mT, applied with a strong toroidal permanent magnet (see Supporting Information Figures S7 and S8). Based on previous reports,[31] this applied field should be enough to switch between stripe domains and uniformly magnetized states; the negligible effect of the magnetic field on $\kappa_\perp$ indicates that the in-plane magnetic domains are not the cause of the sudden change of $\kappa_\perp$ at T_C. We have also discarded as a cause of the jump on $\kappa_\perp$ the eventual changes in the crystal structure since the powder X-ray diffraction of the original bulk crystal revealed only a small change in the *c*-axis lattice parameter and thermal expansion without any crystallographic transformation (Figure 2b). Below T_C, magnons could be an additional source of heat flow, providing an increase in the thermal conductivity; however, the opposite trend is found experimentally, suggesting that heat transport by phonons is the dominant effect in this system, at least for $\kappa_\perp$.

In order to shed light on the observed experimental behavior, we carried out DFT-based calculations on the system. We have studied several magnetic orderings in the system and found that the ground state is the solution where FM layers couple antiferromagnetically. We have computed the temperature dependence of $\kappa_\perp$ in the small-grain limit[32] for the different experimental cases (Figure 5b). The thickness of the flakes was used as the boundary length for the 41 and 22 nm flakes. To identify possible changes at the transition, we have modeled differently the system for temperatures above and below T_C. The ground-state FM solution was considered below T_C, but above T_C, we will consider a nonmagnetic (NM) solution as a possible proxy for the disordered paramagnetic phase above the Curie temperature. Our calculations show an ≈30% drop in the thermal conductivity

https://doi.org/10.1021/acsami.3c11578
ACS Appl. Mater. Interfaces 2023, 15, 49538−49544

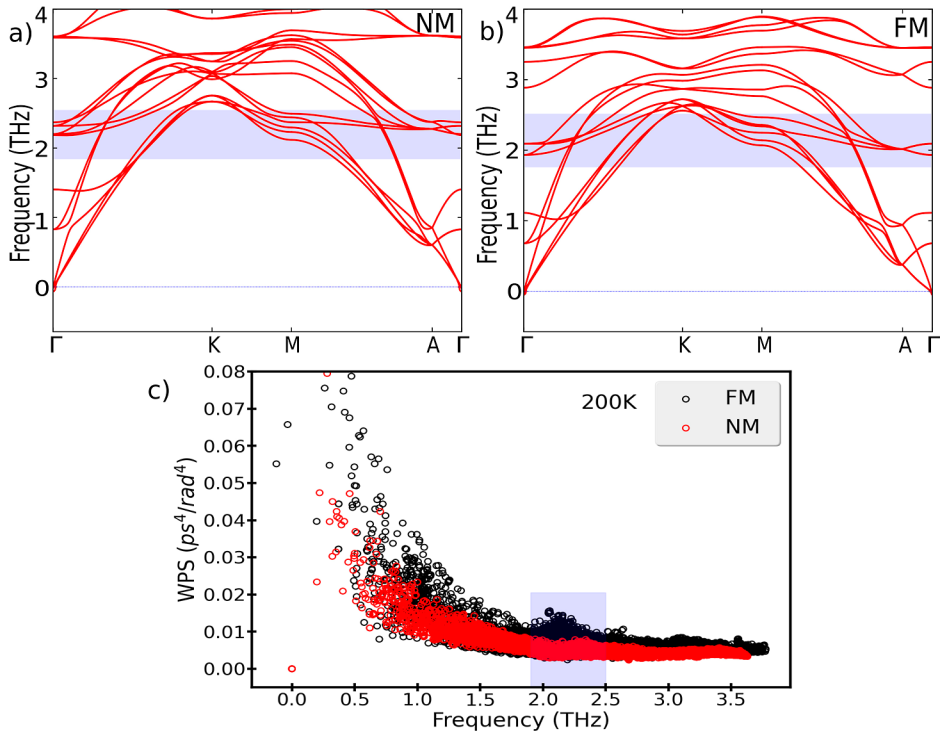

Figure 6. Phonon band diagrams for the magnetic (FM) (a) and non-magnetic (NM) (b) ordering and weighted phase space (WPS) available for three-phonon processes as a function of the frequency (c). The shaded area in (c) corresponds with the highlighted region in both band diagrams. The FM ordering shows an enhanced peak compared to the NM ordering in the WPS around 2.1 THz associated with Raman modes, leading to more scattering processes causing a reduction in the cross-plane thermal conductivity.

between the NM and FM phases in good agreement with the experimental observations. Note that the theoretical underestimation of the thermal conductivity is related to the limitations of the small-grain limit used in the calculations in which the boundary scattering is overestimated, especially at higher temperatures and for larger samples. However, all of the qualitative features are well captured (the change at the transition and also the thickness dependence). Further details about the thickness dependence of the calculations can be found in the Supporting Information.

For understanding the reduction of $\kappa_\perp$ in the magnetic phase, we have analyzed the phonon band structures and the weighted phase space (WPS) available for three-phonon processes for the NM and FM configurations (Figure 6). The WPS gives us an idea of the frequencies involved in phonon scattering processes that are different in the FM and NM states. From the phonon band structures, we can observe that the acoustic phonons undergo a shift toward lower frequencies, especially in the A−Γ path, related to a decrease in group velocities in the out-of-plane direction and hence in the thermal conductivity[33] of the FM phase compared to the NM one discussed above.

Moreover, FM ordering shows an increase in the WPS, specifically a peak around 2 THz that is substantially different from the NM calculation. This peak is related to the phonon modes highlighted in Figure 6a,b and corresponds to two E_{1g} Raman active modes. In the magnetic phase, these modes are about 0.3 THz lower in energy, showing more crossings with the acoustic modes. In the NM calculation, two additional modes appear (an infrared-active A_{2u} mode and a higher-lying B_{1g} mode). These move up to about 3 THz in the FM calculation. The frequency lowering of the modes in the FM calculation leads to the observed additional scattering and causes a reduction in the thermal conductivity.

Strong coupling between Raman-active modes and a particular magnetic order has been reported in other two-dimensional magnets.[34] Here, we observe that, together with the decrease in the group velocities of the acoustic modes, this coupling produces a considerable reduction of the lattice thermal conductivity in the magnetic phase of FGT.

CONCLUSIONS

To summarize, we have combined experimental FDTR and ab initio calculations to demonstrate that the cross-plane thermal conductivity of 2D ferromagnet FGT presents a mixed contribution of diffusive and ballistic phonons. We have also shown that $\kappa_\perp$ presents an abrupt reduction below the Curie temperature due to additional phonon scattering produced by a downshift in the frequency of acoustic and Raman-active optical phonons in the magnetic phase. Also, artificial stacking of a few layer thick FGT is a useful way of reducing the cross-plane thermal conductivity in this material.

EXPERIMENTAL AND COMPUTATIONAL DETAILS

Thermal conductivity was measured by a commercial FDTR from Fourier Inc. using a sinusoidally modulated pump laser (λ = 405 nm, f = 2 kHz to −50 MHz, 1 mW) and a continuous wave 532 nm probe laser (3 mW). Both lasers have Gaussian spot sizes $1/e^2$ with a radius of 3.7 or 10.5 μm. The probe beam is split before reaching the sample to work as a reference signal, improving the signal-to-noise ratio at low frequencies and compensating phase-shift offsets from beam paths and electronics. The same setup is described in detail in the ref 22. A 60 nm gold-thin film deposited by Ar plasma sputtering works as a reflective transducer. The fitting model considers Fourier heat conduction: the heat flux $q = -\kappa\nabla T$, where κ is a tensor to account

https://doi.org/10.1021/acsami.3c11578
ACS Appl. Mater. Interfaces 2023, 15, 49538−49544

for the material thermal conductivity anisotropy. The sample temperature is controlled inside a cold finger optical cryostat, down to 80 K. The whole stage is mounted on a piezoelectric table, which allows μm precision location of the laser spots on the sample. To promote the adhesion of FGT to the sapphire substrate, the samples were annealed under vacuum at 100 °C before the experiments.

$\kappa_\perp$ in the magnetic and nonmagnetic phases of bulk FGT are calculated within a DFT[35,36] framework using the VASP code.[37−39] For all calculations, we performed a full relaxation of the structure (both atomic positions and lattice parameters were optimized) with a mesh of 16 × 16 × 3 k-points in the irreducible wedge of the Brillouin zone. The exchange−correlation potential chosen was the generalized gradient approximation in the Perdew−Burke−Ernzerhof scheme.[40] The second-order interatomic force constants (IFCs) were determined using the Phonopy code[41,42] in a 2 × 2 × 2 supercell with a k-mesh of 8 × 8 × 2 with no further relaxation of cell shape or volume. Third-order anharmonic IFCs were computed using the machinery of the ShengBTE code,[32] considering interactions to third neighbors in a 2 × 2 × 2 supercell. The lattice thermal conductivity was calculated by solving the Boltzmann Transport Equation (BTE) for phonons by an iterative self-consistent method implemented in the ShengBTE code within a mesh of 36 × 36 × 8 q-points and a scale-broad parameter of 0.1.

■ ASSOCIATED CONTENT

Supporting Information

The Supporting Information is available free of charge at https://pubs.acs.org/doi/10.1021/acsami.3c11578.

Additional figures with X-ray powder diffraction pattern of exfoliated crystal,FTDR sensitivity analysis, and details of FDTR measurements with magnetic field (PDF)

■ AUTHOR INFORMATION

Corresponding Authors

Marcel S. Claro − *CiQUS Centro Singular de Investigacion en Quimica Bioloxica e Materiais Moleculares, Departamento de Quimica-Fisica, Universidade de Santiago de Compostela, Santiago de Compostela E-15782, Spain;* orcid.org/0000-0002-4339-7437; Email: marcel.santos@usc.es

Victor Pardo − *Departamento de Física Aplicada and Instituto de Materiais iMATUS, Universidade de Santiago de Compostela, Santiago de Compostela E-15782, Spain;* orcid.org/0000-0002-4713-3519; Email: victor.pardo@usc.es

Authors

Javier Corral-Sertal − *CiQUS Centro Singular de Investigacion en Quimica Bioloxica e Materiais Moleculares, Departamento de Quimica-Fisica, Universidade de Santiago de Compostela, Santiago de Compostela E-15782, Spain*

Adolfo Otero Fumega − *Department of Applied Physics, Aalto University, Aalto FI-00076, Finland;* orcid.org/0000-0002-3385-6409

Santiago Blanco-Canosa − *Donostia International Physics Center (DIPC), San Sebastián E-20018, Spain; IKERBASQUE, Basque Foundation for Science, Bilbao E-48009, Spain*

Manuel Suárez-Rodríguez − *CIC NanoGUNE BRTA, Donostia-San Sebastián E-20018, Spain;* orcid.org/0000-0003-1186-2725

Luis E. Hueso − *CIC NanoGUNE BRTA, Donostia-San Sebastián E-20018, Spain; IKERBASQUE, Basque Foundation for Science, Bilbao E-48009, Spain;* orcid.org/0000-0002-7918-8047

Francisco Rivadulla − *CiQUS Centro Singular de Investigacion en Quimica Bioloxica e Materiais Moleculares, Departamento de Quimica-Fisica, Universidade de Santiago de Compostela, Santiago de Compostela E-15782, Spain;* orcid.org/0000-0003-3099-0159

Complete contact information is available at: https://pubs.acs.org/10.1021/acsami.3c11578

Notes

The authors declare no competing financial interest.

■ ACKNOWLEDGMENTS

This work has received financial support from Ministerio de Economía y Competitividad (Spain), projects PID2019-104150RB-I00 and PID2021-122609NB-C22, Xunta de Galicia (Centro singular de investigación de Galicia accreditation 2019−2022, ED431G 2019/03), and the European Union (European Regional Development Fund-ERDF). We thank the CESGA (Centro de Supercomputación de Galicia for the computational facilities. A.O.F. acknowledges the Academy of Finland Project no. 349696. M.S.C. acknowledges the Maria Zambrano fellowship and NextGenerationEU program. M.S.-R. acknowledges support from La Caixa Foundation (no. 100010434) with code LCF/BQ/DR21/11880030. S.B.-C. acknowledges the MINECO project: PID2021-122609NB-C21.

■ REFERENCES

(1) Novoselov, K. S.; Geim, A. K.; Morozov, S. V.; Jiang, D.; Zhang, Y.; Dubonos, S. V.; Grigorieva, I. V.; Firsov, A. A. Electric Field Effect in Atomically Thin Carbon Films. *Science* **2004**, *306*, 666−669.

(2) Novoselov, K. S.; Geim, A. K.; Morozov, S. V.; Jiang, D.; Katsnelson, M. I.; Grigorieva, I. V.; Dubonos, S. V.; Firsov, A. A. Two-dimensional gas of massless Dirac fermions in graphene. *Nature* **2005**, *438*, 197−200.

(3) Novoselov, K. S.; Jiang, D.; Schedin, F.; Booth, T. J.; Khotkevich, V. V.; Morozov, S. V.; Geim, A. K. Two-dimensional atomic crystals. *Proc. Natl. Acad. Sci. U.S.A.* **2005**, *102*, 10451−10453.

(4) Novoselov, K. S.; Mishchenko, A.; Carvalho, A.; Castro Neto, A. H. 2D materials and van der Waals heterostructures. *Science* **2016**, *353*, aac9439.

(5) Jiang, P.; Qian, X.; Yang, R.; Lindsay, L. Anisotropic thermal transport in bulk hexagonal boron nitride. *Phys. Rev. Mater.* **2018**, *2*, 064005.

(6) Sood, A.; Xiong, F.; Chen, S.; Cheaito, R.; Lian, F.; Asheghi, M.; Cui, Y.; Donadio, D.; Goodson, K. E.; Pop, E. Quasi-Ballistic Thermal Transport Across MoS2 Thin Films. *Nano Lett.* **2019**, *19*, 2434−2442.

(7) Vakulov, D.; Gireesan, S.; Swinkels, M. Y.; Chavez, R.; Vogelaar, T.; Torres, P.; Campo, A.; De Luca, M.; Verheijen, M. A.; Koelling, S.; et al. Ballistic Phonons in Ultrathin Nanowires. *Nano Lett.* **2020**, *20*, 2703−2709.

(8) Kim, S. E.; Mujid, F.; Rai, A.; Eriksson, F.; Suh, J.; Poddar, P.; Ray, A.; Park, C.; Fransson, E.; Zhong, Y.; Muller, D. A.; Erhart, P.; Cahill, D. G.; Park, J. Extremely anisotropic van der Waals thermal conductors. *Nature* **2021**, *597*, 660−665.

(9) Vaziri, S.; Yalon, E.; Muñoz Rojo, M.; Suryavanshi, S. V.; Zhang, H.; McClellan, C. J.; Bailey, C. S.; Smithe, K. K. H.; Gabourie, A. J.; Chen, V.; Deshmukh, S.; Bendersky, L.; Davydov, A. V.; Pop, E. Ultrahigh thermal isolation across heterogeneously layered two-dimensional materials. *Sci. Adv.* **2019**, *5*, No. eaax1325.

(10) Sood, A.; Sievers, C.; Shin, Y. C.; Chen, V.; Chen, S.; Smithe, K. K.; Chatterjee, S.; Donadio, D.; Goodson, K. E.; Pop, E. Engineering Thermal Transport across Layered Graphene-MoS2Superlattices. *ACS Nano* **2021**, *15*, 19503−19512.

(11) Deng, Y.; Yu, Y.; Song, Y.; Zhang, J.; Wang, N. Z.; Sun, Z.; Yi, Y.; Wu, Y. Z.; Wu, S.; Zhu, J.; Wang, J.; Chen, X. H.; Zhang, Y. Gate-

tunable room-temperature ferromagnetism in two-dimensional Fe3GeTe2. *Nature* **2018**, *563*, 94−99.
(12) Du, L.; Tang, J.; Zhao, Y.; Li, X.; Yang, R.; Hu, X.; Bai, X.; Wang, X.; Watanabe, K.; Taniguchi, T.; et al. Lattice Dynamics, Phonon Chirality, and Spin−Phonon Coupling in 2D Itinerant Ferromagnet Fe3GeTe2. *Adv. Funct. Mater.* **2019**, *29*, 1904734.
(13) Wu, C.; Zhao, Y.; Zhang, G.; Liu, C. Giant thermal switching in ferromagnetic VSe_2 with programmable switching temperature. *Nanoscale Horiz.* **2023**, *8*, 202−210.
(14) Qin, G.; Wang, H.; Zhang, L.; Qin, Z.; Hu, M. Giant effect of spin−lattice coupling on the thermal transport in two-dimensional ferromagnetic CrI3. *J. Mater. Chem. C* **2020**, *8*, 3520−3526.
(15) Zhao, X.; Wu, J. C.; Zhao, Z. Y.; He, Z. Z.; Song, J. D.; Zhao, J. Y.; Liu, X. G.; Sun, X. F.; Li, X. G. Heat switch effect in an antiferromagnetic insulator Co3V2O8. *Appl. Phys. Lett.* **2016**, *108*, 242405.
(16) Liu, Y.; Liu, Q.; Liu, Y.; Jiang, X.; Zhang, X.; Zhao, J. Effects of spin−phonon coupling on two-dimensional ferromagnetic semiconductors: a case study of iron and ruthenium trihalides. *Nanoscale* **2021**, *13*, 7714−7722.
(17) Fei, Z.; Huang, B.; Malinowski, P.; Wang, W.; Song, T.; Sanchez, J.; Yao, W.; Xiao, D.; Zhu, X.; May, A. F.; Wu, W.; Cobden, D. H.; Chu, J.-H.; Xu, X. Two-dimensional itinerant ferromagnetism in atomically thin Fe3GeTe2. *Nat. Mater.* **2018**, *17*, 778−782.
(18) May, A. F.; Calder, S.; Cantoni, C.; Cao, H.; McGuire, M. A. Magnetic structure and phase stability of the van der Waals bonded ferromagnet $Fe_{3-x}GeTe_2$. *Phys. Rev. B* **2016**, *93*, 014411.
(19) Yi, J.; Zhuang, H.; Zou, Q.; Wu, Z.; Cao, G.; Tang, S.; Calder, S. A.; Kent, P. R. C.; Mandrus, D.; Gai, Z. Competing antiferromagnetism in a quasi-2D itinerant ferromagnet: Fe3GeTe2. *2D Mater.* **2016**, *4*, 011005.
(20) Spirito, D.; Barra-Burillo, M.; Calavalle, F.; Manganelli, C. L.; Gobbi, M.; Hillenbrand, R.; Casanova, F.; Hueso, L. E.; Martín-García, B. Tailoring Photoluminescence by Strain-Engineering in Layered Perovskite Flakes. *Nano Lett.* **2022**, *22*, 4153−4160.
(21) Tan, C.; Lee, J.; Jung, S.-G.; Park, T.; Albarakati, S.; Partridge, J.; Field, M. R.; McCulloch, D. G.; Wang, L.; Lee, C. Hard magnetic properties in nanoflake van der Waals Fe3GeTe2. *Nat. Commun.* **2018**, *9*, 1554.
(22) Yang, J.; Maragliano, C.; Schmidt, A. J. Thermal property microscopy with frequency domain thermoreflectance. *Rev. Sci. Instrum.* **2013**, *84*, 104904.
(23) Schmidt, A. J.; Cheaito, R.; Chiesa, M. A frequency-domain thermoreflectance method for the characterization of thermal properties. *Rev. Sci. Instrum.* **2009**, *80*, 094901.
(24) Liu, Y.; Li, J.; Tao, J.; Zhu, Y.; Petrovic, C. Anisotropic magnetocaloric effect in Fe3-xGeTe2. *Sci. Rep.* **2019**, *9*, 13233.
(25) Langenberg, E.; Ferreiro-Vila, E.; Leborán, V.; Fumega, A. O.; Pardo, V.; Rivadulla, F. Analysis of the temperature dependence of the thermal conductivity of insulating single crystal oxides. *APL Mater.* **2016**, *4*, 104815.
(26) Zheng, W.; McClellan, C. J.; Pop, E.; Koh, Y. K. Non-equilibrium Phonon Thermal Resistance at MoS_2/Oxide and Graphene/Oxide Interfaces. *ACS Appl. Mater. Interfaces* **2022**, *14*, 22372−22380.
(27) Xiao, P.; Chavez-Angel, E.; Chaitoglou, S.; Sledzinska, M.; Dimoulas, A.; Sotomayor Torres, C. M.; El Sachat, A. Anisotropic Thermal Conductivity of Crystalline Layered SnSe2. *Nano Lett.* **2021**, *21*, 9172−9179.
(28) Li, D.; Gao, J.; Cheng, P.; He, J.; Yin, Y.; Hu, Y.; Chen, L.; Cheng, Y.; Zhao, J. 2D boron sheets: structure, growth, and electronic and thermal transport properties. *Adv. Funct. Mater.* **2020**, *30*, 1904349.
(29) Huang, H.-T.; Lai, M.-F.; Hou, Y.-F.; Wei, Z.-H. Influence of Magnetic Domain Walls and Magnetic Field on the Thermal Conductivity of Magnetic Nanowires. *Nano Lett.* **2015**, *15*, 2773−2779.
(30) Nakayama, H.; Xu, B.; Iwamoto, S.; Yamamoto, K.; Iguchi, R.; Miura, A.; Hirai, T.; Miura, Y.; Sakuraba, Y.; Shiomi, J.; Uchida, K.-i. Above-room-temperature giant thermal conductivity switching in spintronic multilayers. *Appl. Phys. Lett.* **2021**, *118*, 042409.
(31) Birch, M. T.; Powalla, L.; Wintz, S.; Hovorka, O.; Litzius, K.; Loudon, J. C.; Turnbull, L. A.; Nehruji, V.; Son, K.; Bubeck, C.; Rauch, T. G.; Weigand, M.; Goering, E.; Burghard, M.; Schütz, G. History-dependent domain and skyrmion formation in 2D van der Waals magnet Fe3GeTe2. *Nat. Commun.* **2022**, *13*, 3035.
(32) Li, W.; Carrete, J.; A Katcho, N.; Mingo, N. ShengBTE: a solver of the Boltzmann transport equation for phonons. *Comput. Phys. Commun.* **2014**, *185*, 1747−1758.
(33) Fumega, A. O.; Fu, Y.; Pardo, V.; Singh, D. J. Understanding the lattice thermal conductivity of $SrTiO_3$ from an ab initio perspective. *Phys. Rev. Mater.* **2020**, *4*, 033606.
(34) Huang, B.; Cenker, J.; Zhang, X.; Ray, E. L.; Song, T.; Taniguchi, T.; Watanabe, K.; McGuire, M. A.; Xiao, D.; Xu, X. Tuning inelastic light scattering via symmetry control in the two-dimensional magnet CrI3. *Nat. Nanotechnol.* **2020**, *15*, 212−216.
(35) Hohenberg, P.; Kohn, W. Inhomogeneous electron gas. *Phys. Rev.* **1964**, *136*, B864−B871.
(36) Kohn, W.; Sham, L. J. Self-consistent equations including exchange and correlation effects. *Phys. Rev.* **1965**, *140*, A1133−A1138.
(37) Kresse, G.; Hafner, J. Ab initio molecular dynamics for liquid metals. *Phys. Rev. B: Condens. Matter Mater. Phys.* **1993**, *47*, 558−561.
(38) Kresse, G.; Furthmüller, J. Efficiency of ab-initio total energy calculations for metals and semiconductors using a plane-wave basis set. *Comput. Mater. Sci.* **1996**, *6*, 15−50.
(39) Kresse, G.; Furthmüller, J. Efficient iterative schemes for ab initio total-energy calculations using a plane-wave basis set. *Phys. Rev. B: Condens. Matter Mater. Phys.* **1996**, *54*, 11169−11186.
(40) Perdew, J. P.; Burke, K.; Ernzerhof, M. Generalized Gradient Approximation Made Simple. *Phys. Rev. Lett.* **1996**, *77*, 3865−3868.
(41) Togo, A.; Tanaka, I. First principles phonon calculations in materials science. *Scr. Mater.* **2015**, *108*, 1−5.
(42) Togo, A. First-principles Phonon Calculations with Phonopy and Phono3py. *J. Phys. Soc. Jpn.* **2023**, *92*, 012001.

https://doi.org/10.1021/acsami.3c11578
ACS Appl. Mater. Interfaces 2023, 15, 49538−49544